Desalination and Water Treatment
www.deswater.com
doi: 10.5004/dwt.2021.26492

209 (2021) 267–279
January

Enhanced visible light photocatalysis of $Bi_2O_3/BiVO_4$ and Bi_2O_3/Ag_3VO_4 heterojunctions: effects of synthetic procedures

Chung-Hsin Wu[a,*], Cheng-Di Dong[b], Chiu-Wen Chen[b], Yi-Li Lin[c], Syuan-Ru Jhu[a] and Yong-Hui Lin[a]

[a]*Department of Chemical and Materials Engineering, National Kaohsiung University of Science and Technology, 415 Chien Kung Road, Kaohsiung, Taiwan, Tel. +886-7-3814526; Fax: +886-7-3830674; email: wuch@nkust.edu.tw (C.-H. Wu), Tel. +886-7-3814526; emails: f107146119@nkust.edu.tw (S.-R. Jhu), opil123456@gmail.com (Y.-H. Lin)*
[b]*Department of Marine Environmental Engineering, National Kaohsiung University of Science and Technology, Kaohsiung, Taiwan, Tel. 886-7-3617141; emails: cddong@nkust.edu.tw (C.-D. Dong), cwchen@nkust.edu.tw (C.-W. Chen)*
[c]*Department of Safety, Health and Environmental Engineering, National Kaohsiung University of Science and Technology, Kaohsiung, Taiwan, Tel. 886-7-6011000; email: yililin@nkust.edu.tw (Y.-L. Lin)*

Received 2 May 2020; Accepted 23 August 2020

ABSTRACT

In this investigation, different synthetic procedures were used to generate Bi_2O_3 (BOS)/$BiVO_4$ (BVO) and BOS/Ag_3VO_4 (AVO) composites. The BOS/BVO composites that were produced by single-step and two-step processes were denoted as BB1 and BB2, respectively; the BOS/AVO composites that were formed by these processes were denoted as BA1 and BA2, respectively. All photocatalysts were prepared by a hydrothermal process, except for BOS, which was prepared by a solvothermal process. The prepared composites were characterized by X-ray diffraction, scanning electron microscopy, photoluminescence spectroscopy, UV-vis diffuse reflectance spectroscopy, X-ray photoelectron spectroscopy, and specific surface area analysis. C.I. Reactive Red 2 (RR2) was used as the parent compound in photocatalytic reactions to compare the photoactivities of the photocatalysts. The RR2 photodegradation exhibited pseudo-first-order kinetics. Under visible light irradiation, the RR2 photodegradation rate constants of BVO, AVO, BOS, BB1, BB2, BA1, and BA2 were 0.120, 0.168, 0.042, 0.750, 0.354, 1.062, and 1.244 h^{-1}, respectively. The improvement of photocatalytic activity was attributed to the prolongation of the lifetime of photo-generated electron–hole pairs in BOS/BVO and BOS/AVO composites. The findings of this study suggest that the photo-generated holes and superoxide anion radicals are the dominant reactive species in the oxidative degradation of RR2 in the UV/BB2 system; additionally, hydroxyl radicals are the dominant oxidative species in the UV/BA2 system.

Keywords: $BiVO_4$; Ag_3VO_4; Bi_2O_3; Heterojunction; Hydrothermal; Photocatalysis

1. Introduction

Semiconductor photocatalysis has been regarded as an ideal green technology for removing organic pollutants from wastewater. Recently, more and more attention has been paid to the use of photocatalysts for environmental purification and energy conservation. The natural solar spectrum consists of near-infrared, visible (Vis.), and ultraviolet (UV) light [1]. Researchers have devoted much effort to the fabrication of Vis.-driven photocatalysts for use in the treatment of wastewater. The ideal photocatalyst should have a low band gap, high dispersibility, non-toxicity, resistance to

* Corresponding author.

photo-corrosion, and outstanding photocatalytic activity in the degradation of pollutants under Vis. illumination.

$BiVO_4$ (BVO) is an *n*-type semiconductor with high chemical stability and photo-stability. The photocatalytic behavior of pure BVO must be improved because of the rapid recombination of photo-induced carriers therein [2,3]. Ag_3VO_4 (AVO) is another *n*-type semiconductor, which has a narrower band gap and has attracted considerable attention as a potentially useful photocatalyst. However, AVO has some inherent shortcomings, such as low charge separation and high photo-corrosion [4]. Both BVO and AVO must therefore be modified to increase their photoactivity.

The formation of semiconductor composites can enhance charge separation relative to that in its constituents and slow down the recombination of photo-induced electron–hole pairs, which has been intensively studied [5,6]. The combination of *p*- and *n*-type semiconductors is most effective in this regard because such a combination forms a *p*–*n* heterojunction. The *p*–*n* heterojunction, with an internal electric field, can significantly promote the separation of photo-generated charge carriers and improve degradation efficiency [7]. To overcome the shortcoming of BVO and AVO, the combination of BVO and AVO with another semiconductor to form a *p*–*n* heterojunction has been proposed, with the aim of improving electron–hole pair separation and interfacial charge transfer efficiency, to increase photocatalytic activity.

BVO can be coupled with various semiconductors, such as TiO_2 [8–10], $BiFeO_3$ [11,12], $CuInS_2$ [13], CuS [14], Bi_2WO_6 [15], WO_3 [16], AgI [17], β-FeOOH [18], $FeVO_4$ [19], $InVO_4$ [20,21], BiOCl [22], WO_3 [23], $BiFeWO_6$ [24], Bi_2O_3 (BOS) [3,25–30], Ag_2S [31], and Ag_3VO_4 [32] to improve its photocatalytic activity. Mao et al. [26] synthesized BVO/BOS composite using a solvothermal method followed by annealing. Qui et al. [28] prepared BVO/BOS composite by a chemical bath deposition method, followed by calcination treatment in an N_2 atmosphere. Sun et al. [29] generated BVO/BOS composite using a simple one-pot hydrothermal method. Li and Yan [25] prepared BVO/BOS heterojunctions by directly mixing two semiconductors. The enhanced photocatalytic activity thus achieved was attributed to the larger specific surface areas, outstanding charge migration, and electron–hole separation of the BVO/BOS composites.

Heterojunctions that comprise AVO in combination with other semiconductors have potentially a wide range of applications because they can effectively separate photogenerated charges and improve photocatalytic performance; these include $CoTiO_3$ [33], Ag_2MoO_4 [34], Co_3O_4 [35], NiO [36], g-C_3N_4 [37], $MgFe_2O_4$ [38], $NiTiO_3$ [39], BOS [4], Bi_2WO_6 [40], $BiOIO_3$ [41], and Rb_xWO_3 [1]. The formation of a heterojunction between a photocatalyst and AVO increases the Vis.-harvesting ability of the composite and provides efficient photo-generated hole–electron separation, which results in the generation of many active species in the hybrid system and consequently excellent photocatalytic activity.

Recently, the *p*-type BOS semiconductor, as the simplest bismuth oxide, has attracted much attention owing to its numerous favorable properties, such as wide band gap range (2.0–3.96 eV), good electrochemical performance, and high oxygen-ion conductivity [29]. Accordingly, in this study, BOS will be combined with BVO or AVO to form a *p*–*n* heterojunction to promote the photoactivity of BVO or AVO. Since the synthetic method and procedure influenced the photocatalytic activity and morphology of a photocatalyst [2], single-step and two-step processes will be used herein to synthesize BOS/BVO and BOS/AVO composites. The objectives of this work are (i) to compare the effects of the procedures for synthesizing BOS/BVO and BOS/AVO composites on photocatalytic activity; (ii) to determine the surface characteristics of the prepared photocatalysts; and (iii) to propose possible mechanisms by which the photoactivities of BOS/BVO and BOS/AVO composites are enhanced.

2. Materials and methods

2.1. Materials

Bismuth nitrate ($Bi(NO_3)_3{\cdot}5H_2O$), ammonium metavanadate (NH_4VO_3), trisodium citrate (TCD, $Na_3C_6H_5O_7{\cdot}2H_2O$), NaOH, HNO_3, disodium ethylenediamine tetraacetate (EDTA-2Na, $C_{10}H_{14}N_2O_8Na_2{\cdot}2H_2O$), and potassium chromate (K_2CrO_4) were all purchased from Katayama (Japan). Sodium orthovanadate (Na_3VO_4) was obtained from Alaf-Aesar (USA). Silver nitrate ($AgNO_3$), sodium nitrite ($NaNO_2$), and C.I. Reactive Red 2 (RR2, $C_{19}H_{10}Cl_2N_6Na_2O_7S_2$) were all obtained from Sigma Aldrich (USA). Ethylene glycol (EG) and isopropanol (IPA) were purchased from J.T. Baker (USA). All reagents were of analytical grade and used without further purification. Deionized water (D.I. water) was used throughout this study.

2.2. Procedures for synthesizing photocatalysts

BVO, AVO, BOS/BVO, and BOS/AVO composites were all prepared using a hydrothermal process. BOS was generated by a solvothermal process.

2.2.1. BVO

The procedures for synthesizing BVO were modified from those used by Wu et al. [3], and the details are as follows. 2.4745 g of $Bi(NO_3)_3{\cdot}5H_2O$ was added to 60 mL 2 M HNO_3 to form solution A. 0.5850 g of NH_4VO_3 was dissolved in 60 mL 2 M NaOH to yield solution B. 0.4456 g of TCD was dissolved in 20 mL D.I. water t.o form solution C. Solutions A, B, and C were mixed and adjusted to pH 1 by adding 10 M NaOH or HNO_3 and stirred (600 rpm) for 30 min. The adjusted mixture was sealed in a 200 mL Teflon-lined stainless steel autoclave and heated at 473 K under self-generated pressure for 12 h; it was then allowed to cool naturally to room temperature. Resulting precipitates were collected by filtration and washed using 50 mL 95% ethanol and 100 mL D.I. water to remove any residual impurities. The samples were finally dried in air at 333 K for 24 h to yield BVO.

2.2.2. AVO

The procedures for synthesizing AVO were modified from those used by Wu et al. [4], and the details are as follows. 2.5845 g of $AgNO_3$ and 0.9205 g of Na_3VO_4 were dissolved in 60 mL D.I. water to yield solutions A and B, respectively. 0.4456 g of TCD was dissolved in 20 mL D.I. water to form solution C. Solutions A, B, and C were mixed

and adjusted to pH 13 by adding 10 M NaOH or HNO_3 and stirring (600 rpm) for 30 min. The adjusted mixture was sealed in a 200 mL Teflon-lined stainless autoclave and maintained at 393 K for 6 h. The subsequent steps and conditions for the formation of AVO were as for BVO.

2.2.3. BOS

A 4.949 g mass of $Bi(NO_3)_3{\cdot}5H_2O$ was added to 110 mL EG to form solution A. Thirty milliliters D.I. water was added to solution A, whose pH was then adjusted to pH 1 by adding 10 M NaOH or HNO_3 and stirring (600 rpm) for 30 min. The solution was sealed in a 200 mL Teflon-lined stainless steel autoclave and heated at 473 K under self-generated pressure for 12 h. The subsequent procedures and conditions for generating BOS were those used in generating BVO.

2.2.4. BOS/BVO composites

The BOS/BVO composite that was prepared by a single-step hydrothermal process was denoted as BB1 and that prepared by a two-step was denoted as BB2. Both BB1 and BB2 had a BOS/BVO molar ratio of unity. The procedure for producing BB1 was as follows. 7.4235 g of $Bi(NO_3)_3{\cdot}5H_2O$ was added to 60 mL 2 M HNO_3 to form solution A. 0.5850 g of NH_4VO_3 was dissolved in 60 mL 2 M NaOH to yield solution B. 0.4456 g of TCD was dissolved in 20 mL D.I. water to form solution C. The procedures and conditions that were subsequently used to obtain BB1 were those used to obtain BVO. To synthesize BB2, the prepared BOS particles were added to the solution of BVO precursors. The subsequent procedures and conditions that were used to generate BB2 were the same as those used to generate BVO.

2.2.5. BOS/AVO composites

BOS/AVO composite that was prepared using a single-step hydrothermal process was denoted as BA1 and that prepared by a two-step process was denoted as BA2. Both BA1 and BA2 had a BOS/AVO molar ratio of unity. The procedure for producing BA1 was as follows. 2.5845 g of $AgNO_3$ and 0.9205 g of Na_3VO_4 were dissolved in 30 mL D.I. water to yield solutions A and B, respectively. 0.4456 g of TCD was dissolved in 20 mL D.I. water to form solution C. 4.9192 g of $Bi(NO_3)_3{\cdot}5H_2O$ was added to 60 mL 2 M HNO_3 to form solution D. The solutions A, B, C, and D were mixed and adjusted to pH 7 by adding 10 M NaOH or HNO_3 and stirring (600 rpm) for 30 min. The subsequent procedures and conditions for producing BA1 were same as those for producing AVO. To synthesize BA1, the prepared BOS particles were added to the solution of AVO precursors. The subsequent procedures and conditions for generating BA2 were the same as those for generating AVO.

2.3. Analyses of surface characteristics

The crystalline phase of the prepared photocatalysts was characterized by X-ray diffraction (XRD) with Cu-Kα radiation (Bruker D8 SSS, Germany) over a 2θ range 20°–70°. The morphology and size of the prepared photocatalysts were observed using scanning electron microscopy (SEM, JEOL 6330 TF, Japan). The band gap was calculated from the diffuse reflectance UV-vis. spectra of the photocatalysts, which were obtained using a UV-vis spectrophotometer (JAS.CO-V670, Japan). The photoluminescence (PL) spectra were measured using an excitation wavelength of 400 nm and a Hitachi F-4500 fluorescence spectrophotometer (Japan). The Brunauer–Emmett–Teller (BET) surface area was determined from the N_2 adsorption–desorption isotherm using the Barrer–Joyner–Halenda (BJH) technique with a Micrometrics ASAP 2020 surface area analyzer (USA). X-ray photoelectron spectroscopy (XPS) measurements were made at room temperature using a PHI 5000 Versal Probe X-ray photoelectron spectrometer (USA). All of the binding energies were calibrated against that of the surface adventitious carbon (C 1s), 284.6 eV, as the reference. Valence band XPS was used to estimate the position of the valence band edge. The concentration of Ag that leached from photocatalysts during photodegradation was measured by inductively coupled plasma-optical emission spectrometry (ICP-OES, Perkin Elmer Optima 5300DV, USA).

2.4. Photocatalysis experiments

The photocatalyst dosage, RR2 concentration and temperature in all of the experiments were 0.5 g/L, 20 mg/L, and 298 K, respectively. The solution pH was 3 in all experiments except those performed to determine the effects of pH. Photocatalysis experiments were conducted in a 3 L glass reactor. The light source was a 400 W Xe lamp (200 nm < wavelength < 700 nm, UniVex BT-580, Taiwan) and the intensity of light from the lamp was 30.3 mW/cm^2. A quartz appliance that was filled with 2 M $NaNO_2$ solution was placed on top of the reactor to cut the UV and to provide Vis. [42]. Adsorption experiments were carried out in darkness. The reaction medium was stirred continuously at 300 rpm and aerated with air to maintain a suspension. Following sampling at specific intervals, solids were separated by filtration through a 0.22 μm filter (Millipore, USA), and the RR2 concentration that remained in the filtrate was analyzed by measuring its absorbance at 538 nm using a spectrophotometer (Hitachi U-5100, Japan). The used AVO, BA1, and BA2 were denoted as AVO(R), BA1(R), and BA2(R), respectively. To identify the main active species in the photocatalytic system, ethylene diamine disodium salt (EDTA-2Na), isopropyl alcohol (IPA), and potassium chromate (Cr(VI)), which scavenge the active species of photo-generated holes (h^+) [43,44], hydroxyl radicals ($^{\bullet}OH$) [43,44], and superoxide anion radicals ($^{\bullet}O_2^-$) [45], respectively, were added separately to the photocatalytic reaction. The experiments were performed in triplicate and mean values of results reported.

3. Results and discussion

3.1. Determination of crystal properties

Fig. 1 presents the XRD patterns of all prepared photocatalysts, which exhibit several broad diffraction peaks that are characteristic of monoclinic BVO (JCPDS 14-0688), monoclinic AVO (JCPDS 43-0542), and BOS (JCPDS 51-1161) crystals. The sharp and intense diffraction peaks of all particles revealed that the samples were well crystallized.

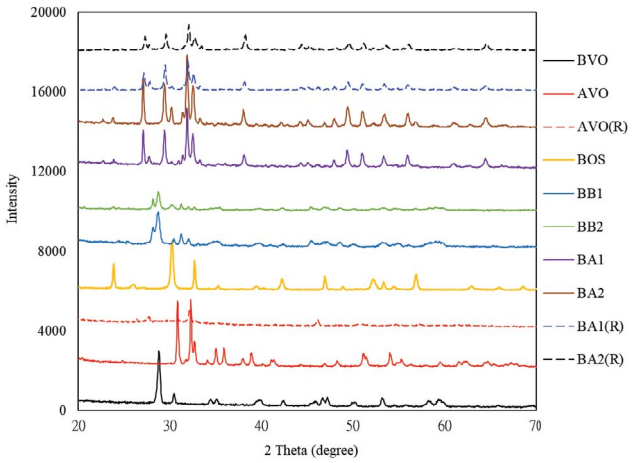

Fig. 1. XRD patterns of all prepared photocatalysts.

The strongest characteristic diffraction peaks from BVO and BOS were at 28.8° and 30.2°, respectively, and those from AVO were at 30.9° and 32.3°. For BB1, BB2, BA1, and BA2, the characteristic peaks of BVO, AVO, and BOS were shifted to slightly lower 2θ angles. The composites yielded the diffraction peaks of BVO, AVO, and BOS, suggesting the formation of BOS/BVO and BOS/AVO composites. The shift might have been caused by the partial doping of BVO (or AVO) into the BOS lattice.

3.2. Determinations of surface properties

The morphologies of the synthesized photocatalysts were determined using SEM (Fig. 2). The BVO, AVO, and BOS crystals had peanut-like, spherical, and flake-like morphologies, as shown in Figs. 2a–c, respectively. Figs. 2d and e show that BVO powders were immobilized by BOS sheets; additionally, Figs. 2f and g show that AVO particles were immobilized by BOS sheets. SEM images in Figs. 2d–g also show that some BVO and AVO particles were attached to the BOS sheets, further revealing that the composites had been successfully fabricated. All prepared samples exhibited considerable degrees of agglomeration.

The absorption of Vis. is important in evaluating Vis.-driven photocatalytic activity. Fig. 3 presents UV-vis absorption spectra of photocatalysts. All photocatalysts absorbed in the Vis. region. The band gap between the valence band (VB) and the conduction band (CB) of all photocatalysts is estimated using λ (nm) = 1,240/E_g (eV), where λ and E_g are the absorption band threshold wavelength and the band gap, respectively. The E_g values of BVO, AVO, BOS, BB1, BB2, BA1, and BA2 are calculated to be approximately 2.3, 1.8, 3.4, 2.4, 2.3, 2.4, and 2.4 eV, respectively, and their respective BET surface areas are 0.03, 0.67, 9.58, 8.42, 2.87, 0.31, and 0.16 m^2/g (Table 1).

PL spectra are extensively used to identify the migration, transfer, and recombination processes of photogenerated electron–hole pairs in photocatalysts. A lower PL intensity may imply a lower recombination rate of electron–hole pairs under light irradiation. Fig. 4 plots the PL spectra of BVO, AVO, BOS, BB1, and BA1. BA1 had the lowest PL intensity (Fig. 4), revealing separation of the photogenerated electrons and holes therein and inhibition of the recombination of the electrons and hole pairs, increasing photocatalytic activity [46,47].

XPS was used to measure the binding energy of chemical bonds and the surface chemical composition of BB1 and BA1 heterojunctions. The spectra confirm the presence of Bi, V, and O in BB1 (Fig. 5), as well as Bi, V, Ag, and O in BA1 (Fig. 6). The Bi $4f_{5/2}$ and Bi $4f_{7/2}$ peaks at 162.6–163.7 and 157.2–158.2 eV, respectively, are consistent with Bi^{3+} (Figs. 5a and 6a) [48,49]. The V $2p_{3/2}$ and V $2p_{1/2}$ peaks at 515.5 and 522.7 eV confirm the presence of V^{5+} (Figs. 5b and 6b) [41,48]. The Ag $3d_{5/2}$ and Ag $3d_{3/2}$ peaks at 367.7 and 373.7 eV are characteristic of Ag^+ (Fig. 6c) [1,40,41]. No Ag^0 is identified by peak fitting. The O 1s peaks of BB1 at 528.5, 529.9, and 531.2 eV (Fig. 5c) are attributed to Bi–O [49], V–O [50], and –OH [51] bonds, respectively. The O 1s peaks of BA1 at 528.9, 528–529.3, 529.9, and 531.2 eV (Fig. 6d) are attributed to Ag–O [52], Bi–O [49,53], V–O [50], and –OH [51] bonds, respectively.

3.3. Evaluation of photoactivities of prepared photocatalysts

Fig. 7 displays the concentrations of RR2 removed by all prepared photocatalysts. The efficiencies of removal of RR2 after 60 min of adsorption by BVO, AVO, BOS, BB1, BB2, BA1, and BA2 were 16%, 8%, 8%, 30%, 14%, 15%, and 19%, respectively (Fig. 7a). RR2 cannot be effectively decolorized by adsorption. After 60 min of reaction, the percentages of RR2 that were removed by BVO, AVO, BOS, BB1, BB2, BA1, and BA2 with UV photocatalysis were 35%, 94%, 91%, 78%, 45%, 87%, and 84%, respectively (Fig. 7b), and with Vis. photocatalysis were 22%, 22%, 12%, 60%, 35%, 65%, and 71%, respectively (Fig. 7c). The photodegradation of RR2 can be regarded as following pseudo-first-order kinetics, and the reaction can therefore be expressed using the formula $\ln(C_0/C) = kt$, where C_0 and C are the initial concentration of RR2 and the concentration of RR2 at a reaction time of t, respectively, and k is the pseudo-first-order rate constant. A strongly linear relationship was observed between $\ln(C_0/C)$ and irradiation time (Table 2). Under UV irradiation, the k values followed the order AVO > BA1 > BA2 > BOS > BB1 > BB2 > BVO, while under Vis. illumination, they obeyed the order BA2 > BA1 > BB1 > BB2 > AV O > BVO > BOS. Under Vis. irradiation, the degradation rates of RR2 in BB1 and BB2 heterojunctions were 6.25 and 2.95 times higher than that in bare BVO, respectively; those in BA1 and BA2 heterojunctions were 6.32 and 7.29 times higher than that in bare AVO, respectively. The outstanding Vis. photocatalytic performance of BOS/BVO and BOS/AVO composites is attributable to the synergistic effect of BOS and BVO (or AVO). Under Vis. irradiation, the degradation rate of RR2 in the BB1 heterojunction was 7.8 times higher than that in a mechanical mixture of BVO and BOS, while in the BA1 heterojunction, it was 4.1 times higher than that in a mechanical mixture of AVO and BOS (Table 2). Therefore, the formation of a *p–n* heterojunction was critical to the enhancement of Vis. photocatalysis. The improvement of photocatalytic activity is attributed to the prolongation of the lifetime of photo-generated electron-hole pairs in BOS/BVO and BOS/AVO composites.

The RR2 photodegradation performance at pH 3 exceeded that at pH 9 (Table 2) owing to the change in

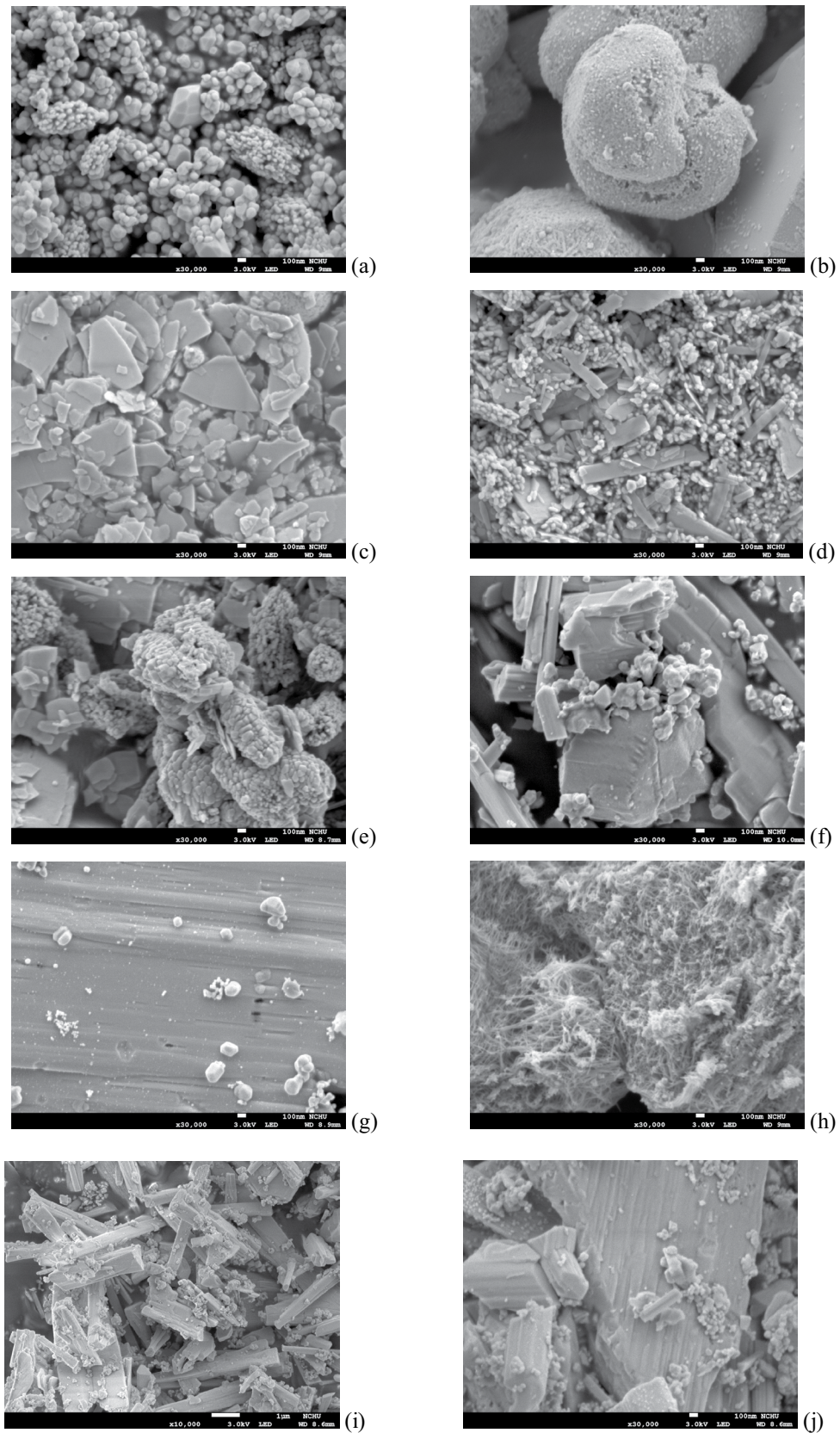

Fig. 2. SEM image of photocatalyst (a) BVO, (b) AVO, (c) BOS, (d) BB1, (e) BB2, (f) BA1, (g) BA2, (h) AVO(R), (i) BA1(R), and (j) BA2(R).

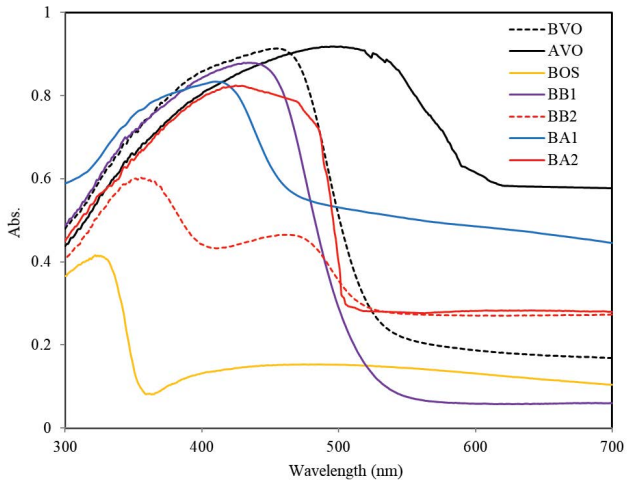

Fig. 3. UV-vis absorption spectra of prepared photocatalysts.

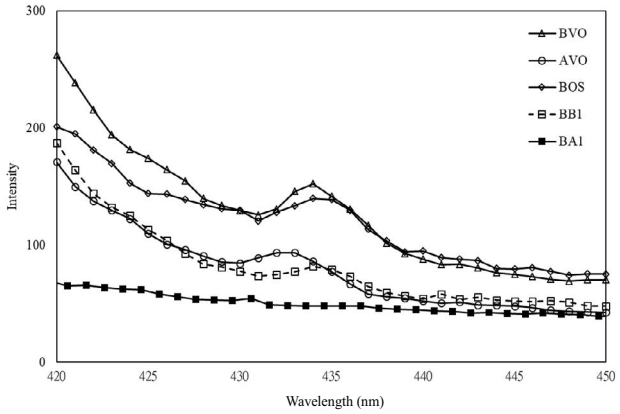

Fig. 4. PL spectra of BVO, AVO, BOS, BB1, and BA1.

Table 1
Surface characteristics of prepared photocatalysts

Photocatalysts	BET surface area (m^2/g)	Band gap (eV)	*X* (eV)	CB (eV)	VB (eV)
BVO	0.03	2.3	6.04*	0.39	2.69
AVO	0.67	1.8	5.65**	0.25	2.05
BOS	9.58	3.4	5.95*	–0.25	3.15
BB1	8.42	2.4	–	–	–
BB2	2.87	2.3	–	–	–
BA1	0.31	2.4	–	–	–
BA2	0.16	2.4	–	–	–

*Chen et al. [54]
**Li et al. [56]

Table 2
Photocatalysis rate constants and linear coefficients of RR2 in different systems ([RR2] = 20 mg/L, [photocatalyst] = 0.5 g/L, and pH = 3)

Systems	Round 1		Round 2		Round 3	
	k (h^{-1})	R^2	k (h^{-1})	R^2	k (h^{-1})	R^2
UV/BVO	0.432	0.998	–	–	–	–
Vis./BVO	0.120	0.990	–	–	–	–
UV/AVO	5.124	0.958	–	–	–	–
Vis./AVO	0.168	0.852	–	–	–	–
UV/BOS	2.262	0.996	–	–	–	–
Vis./BOS	0.042	0.848	–	–	–	–
UV/BB1	1.446 (0.312)*	0.998	0.996	0.999	0.810	0.995
UV/BB2	0.384 (0.096)*	0.989	0.336	0.990	0.324	0.992
Vis./BB1	0.750 (0.096)**	0.998	0.630	0.990	0.606	0.981
Vis./BB2	0.354	0.987	0.336	0.956	0.312	0.949
UV/BA1	3.996	0.944	3.744	0.886	3.384	0.989
UV/BA2	3.264	0.989	2.058	0.977	2.022	0.976
Vis./BA1	1.062 (0.258)**	0.999	1.008	0.995	0.692	0.963
Vis./BA2	1.224	0.996	0.930	0.914	0.960	0.946

*(): at pH 9
**(): physical mixing

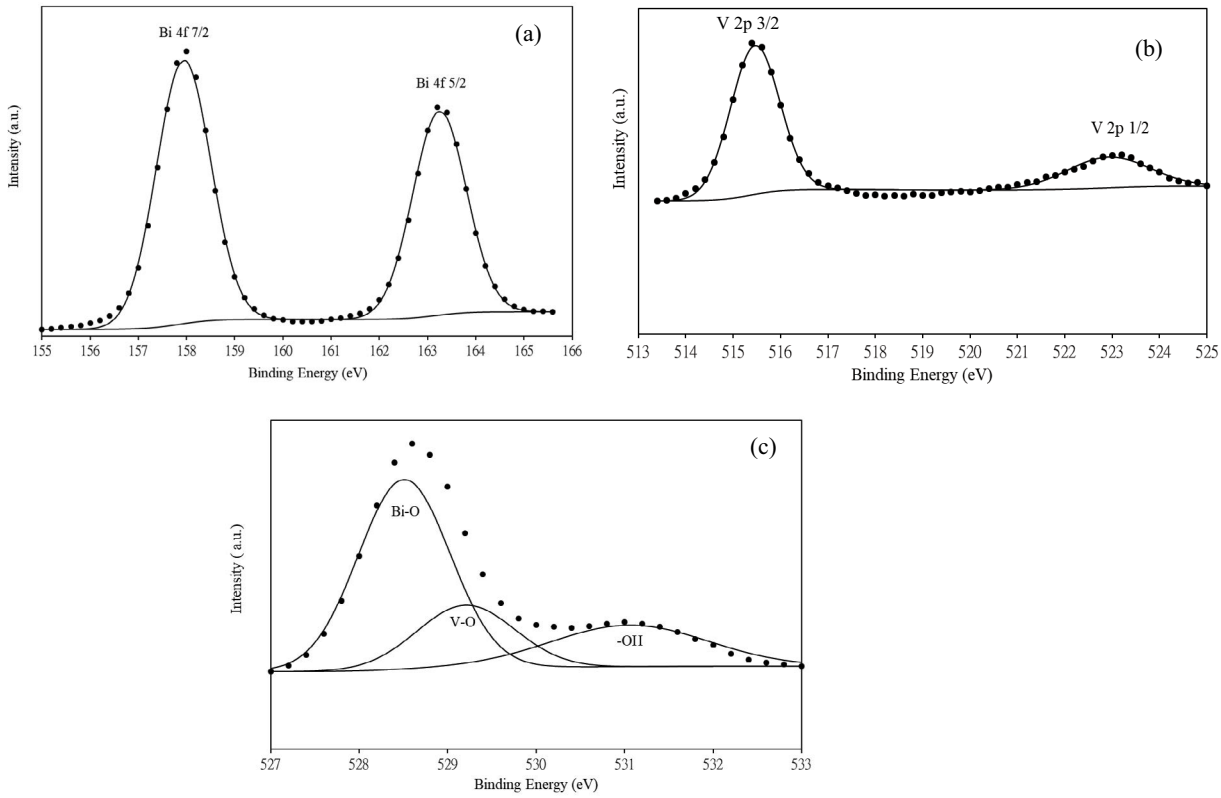

Fig. 5. XPS spectra of BB1 (a) Bi 4f, (b) V 2p, and (c) O 1s.

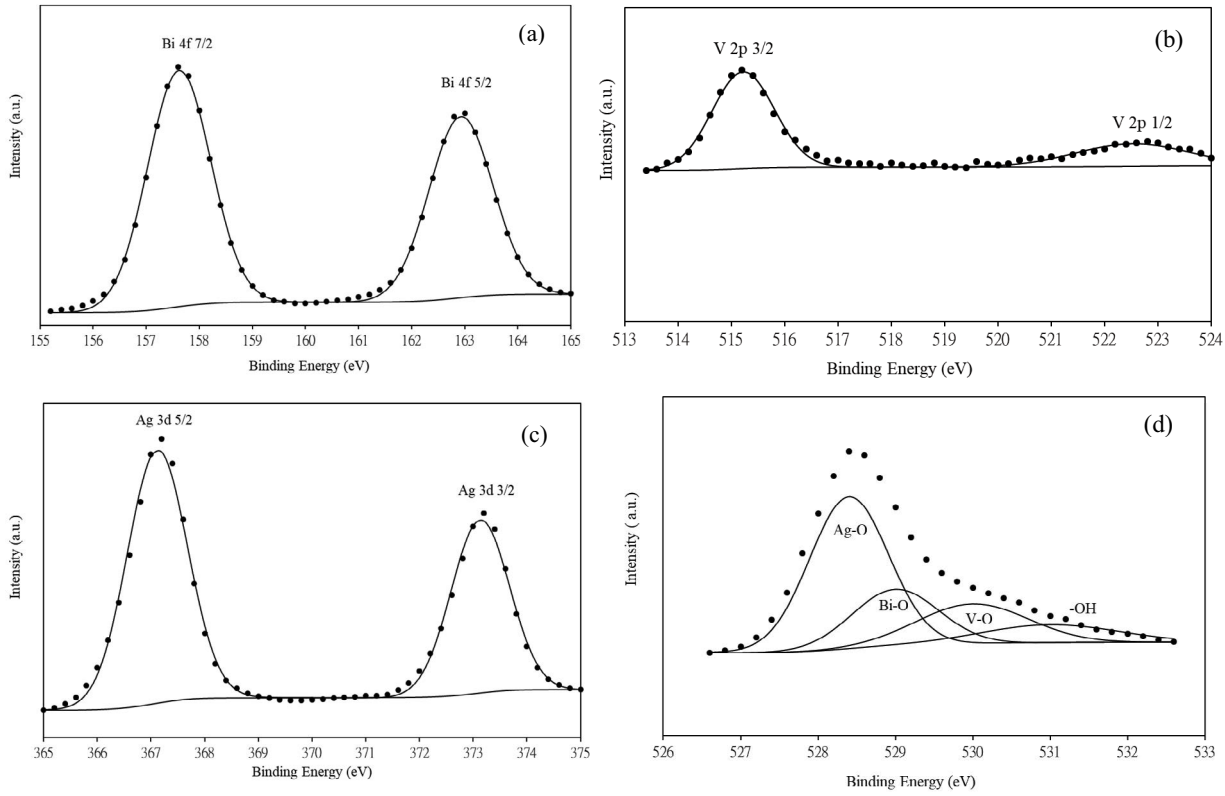

Fig. 6. XPS spectra of BA1 (a) Bi 4f, (b) V 2p, (c) Ag 3d, and (d) O 1s.

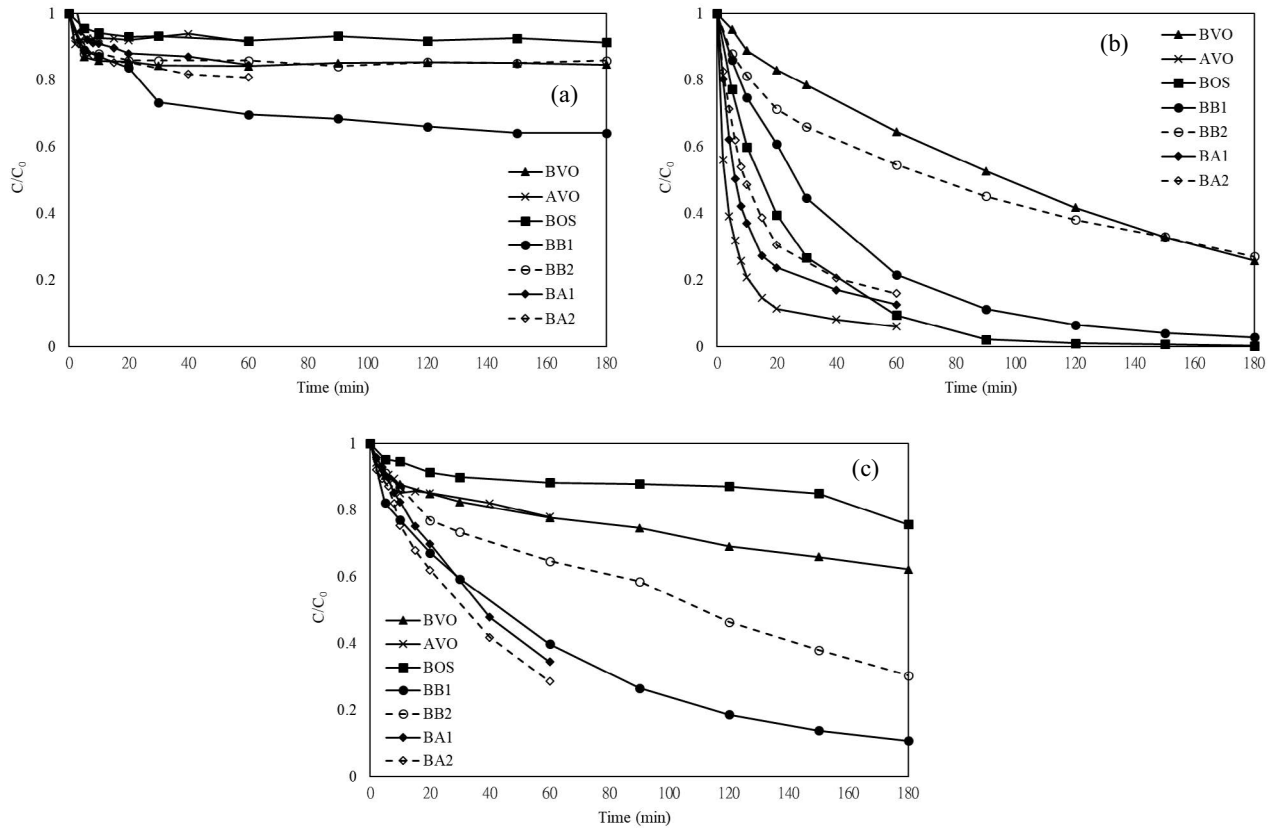

Fig. 7. Comparisons of RR2 removal by all photocatalysts (a) adsorption, (b) UV photocatalysis, and (c) Vis. photocatalysis ([RR2] = 20 mg/L, pH = 3, and [photocatalyst] = 0.5 g/L).

electrostatic attraction or repulsion between RR2 and the photocatalyst. RR2 is an anionic dye so the electrostatic attraction between RR2 molecules and the photocatalyst was much greater at pH 3. Additionally, at a high pH value, the negatively charged photocatalyst surface prevented the sorption of hydroxide ions, reducing the formation of $^{\bullet}OH$ and the photocatalytic activity.

After each run, the photocatalyst was collected, washed using D.I. water to remove residual RR2, dried at 353 K, and then put into fresh RR2 solution to begin a new cycle. In the recycling experiments, all experimental conditions were exactly the same as in the first cycle; the results are presented in Fig. 8. The photo-stability and reusability of the photocatalysts are vital considerations for their practical application, because photo-corrosion strongly limits their stability. The experimental results at the end of three cycling runs revealed that the photocatalytic activities of BB1, BB2, and BA1 were up to 85% of those in the first cycle (Fig. 8). The photocatalytic activity drops slightly in the third cycle perhaps due to the leaching of Ag from AVO or the blocking by some byproducts that were formed at the active sites of the photocatalysts during photocatalysis. Zhang and Ma [40,41] observed the transformation of some surface Ag^{+} to Ag^{0} during the recycling test, probably as a result of photo-corrosion of the photocatalyst. Accordingly, photo-corrosion of the photocatalyst might be responsible for the slight drop in photocatalytic activity. The k values of all systems followed the order round 1 > round 2 > round 3 (Table 2).

The XRD patterns in Fig. 1 revealed a noticeable decrease in the intensity of the peaks from the crystal structures of the used photocatalysts. The intensities of the peak at 32.3° (for AVO) followed the order AVO > BA1(R) > BA2(R) > AVO(R). These results reveal that the AVO exhibited exceptional instability and was seriously affected by photo-corrosion in the photocatalytic reactions. Accordingly, AVO cannot be used for long-term photodegradation. The coupling of BOS with AVO reduced the Ag leaching concentration from 352 to 3 mg/L after 60 min of photocatalysis. Before photocatalysis, the AVO crystal had a sphere-like morphology (Fig. 2b), whereas after photocatalysis, AVO(R) had a fluffy morphology, as shown in Fig. 2h. The SEM images of BA1(R) (Fig. 2i) and BA2(R) (Fig. 2j) were similar to those of BA1 and BA2 before photocatalysis. The results of XRD, SEM, Ag leaching, and photocatalysis proved that coupling AVO with BOS increased the photocatalytic activity and reusability of AVO. BOS, BVO, and BOS/BVO composites did not suffer from Bi leaching during photocatalysis.

To identify the main active species that were generated in the UV/BB2 and UV/BA2 systems, radical-trapping measurements were made. Fig. 9a shows the effects of scavenger addition on the photodegradation of RR2 in the UV/BB2 system. Adding IPA had no effect on RR2 photodegradation whereas adding EDTA-2Na and Cr(VI) inhibited it. This work suggested that h^{+} and $^{\bullet}O_2^{-}$ are the dominant reactive species in the oxidative degradation of RR2 in the UV/

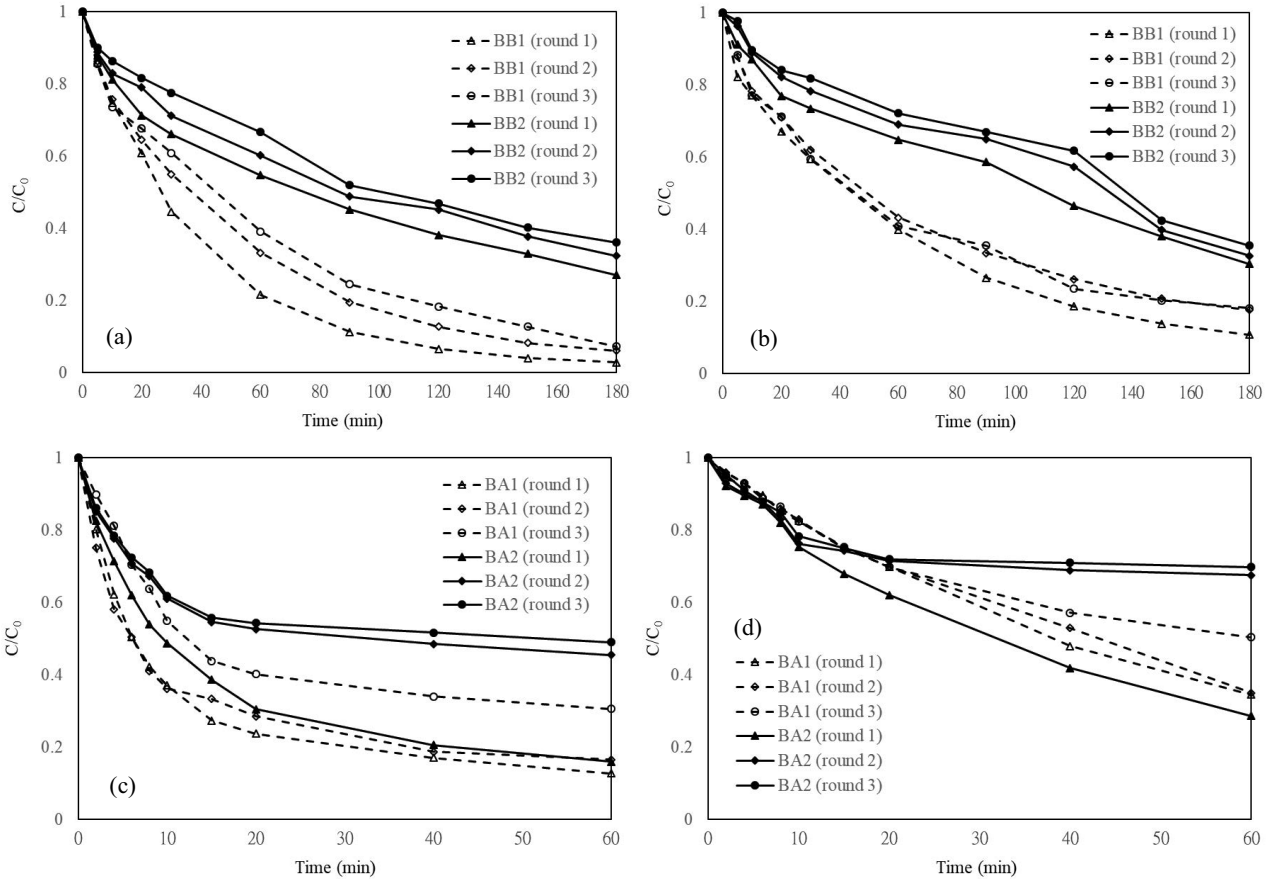

Fig. 8. Comparisons of cyclic photocatalysis in different systems (a) UV/BB, (b) Vis/BB, (c) UV/BA, and (d) Vis/BA ([RR2] = 20 mg/L, pH = 3, and [photocatalyst] = 0.5 g/L).

BB2 system. In contrast, Fig. 9b shows that adding EDTA-2Na and Cr(VI) had no effect on RR2 photodegradation, whereas adding IPA inhibited it. •OH is thus inferred to be the dominant oxidative species in the UV/BA2 system.

3.4. Mechanism of enhancement of photocatalytic efficiency

To understand the separation of the photo-generated charge carriers, the VB and CB energies of BVO, AVO, and BOS at the point of zero charge were calculated using Butler and Ginley equations (Eqs. (1) and (2)) [27,54,55].

$$E_{CB} = X - E_e - 0.5\,E_g \quad (1)$$

$$E_{VB} = E_{CB} + E_g \quad (2)$$

where X is the absolute electronegativity of the photocatalyst. The absolute electronegativity is defined as the arithmetic mean of the atomic electron affinity and the first ionization energy. The X values for BOS and BVO are 5.95 and 6.04 eV, respectively [54], and that for AVO is 5.65 [56]. E_e is the energy of free electrons on the hydrogen scale (4.5 eV); E_g is the band gap of the photocatalyst, and E_{CB} and E_{VB} are the CB and VB edge potentials, respectively [27]. The E_{CB} values of BVO, AVO, and BOS are determined to be 0.39, 0.25, and –0.25 eV relative to the NHE level, respectively. The E_{VB} values of BVO, AVO, and BOS are obtained as 2.69, 2.05, and 3.15 eV, respectively. These band edge positions of the photocatalysts were their potentials before contact.

Based on the measured band gap structures of BVO, AVO, and BOS and the trapping experiments, a mechanism of the enhancement of photocatalytic performance of BB2 and BA2 is proposed. Fig. 10 displays energy band diagrams and possible charge-separation processes of UV/BB2 and UV/BA2 systems. BOS is an intrinsic *p*-type semiconductor with a high hole mobility, so can serve as an electron donor in a photocatalyst. BVO and AVO are intrinsic *n*-type semiconductors, and can act as electron acceptors, providing a pathway for interfacial charge transfer. This difference between CB and VB potentials establishes a potential difference across the interface of the two photocatalysts, forming a heterojunction. Therefore, when BVO (or AVO) and BOS shells are in contact with each other, their band structures are reconfigured. The energy bands of the BOS and BVO (or AVO) shift upward and downward, respectively, with the diffusion of charge carriers until the Fermi levels of BOS and BVO (or AVO) reach equilibrium [28]. The newly formed band structure has a lower potential of oxidation and a higher potential of reduction, greatly increasing both oxidative, and reductive capacities [30]. The efficient separation of photo-generated electron–hole

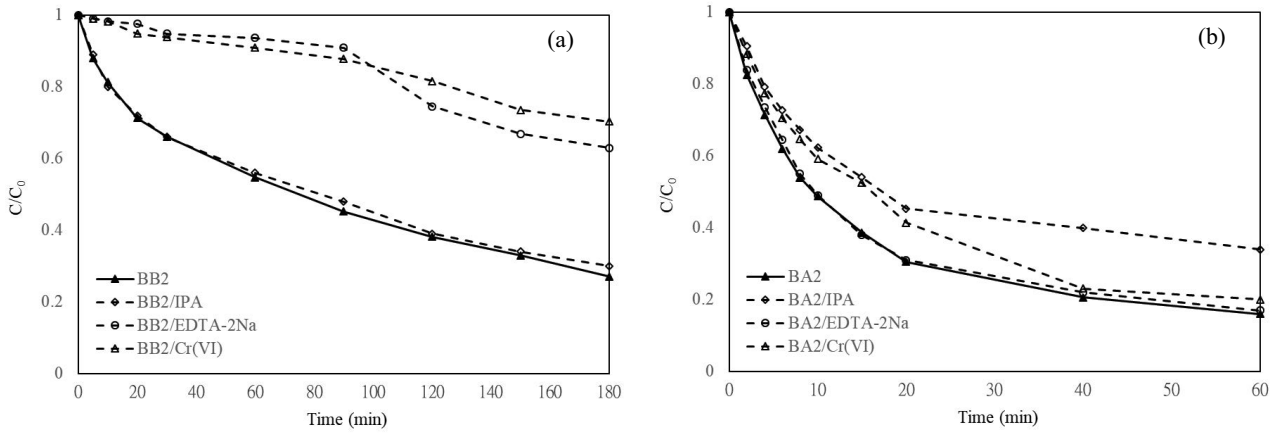

Fig. 9. Photocatalysis of RR2 in presence of scavengers for different systems (a) UV/BB2 and (b) UV/BA2 ([RR2] = 20 mg/L, pH = 3, and [photocatalyst] = 0.5 g/L).

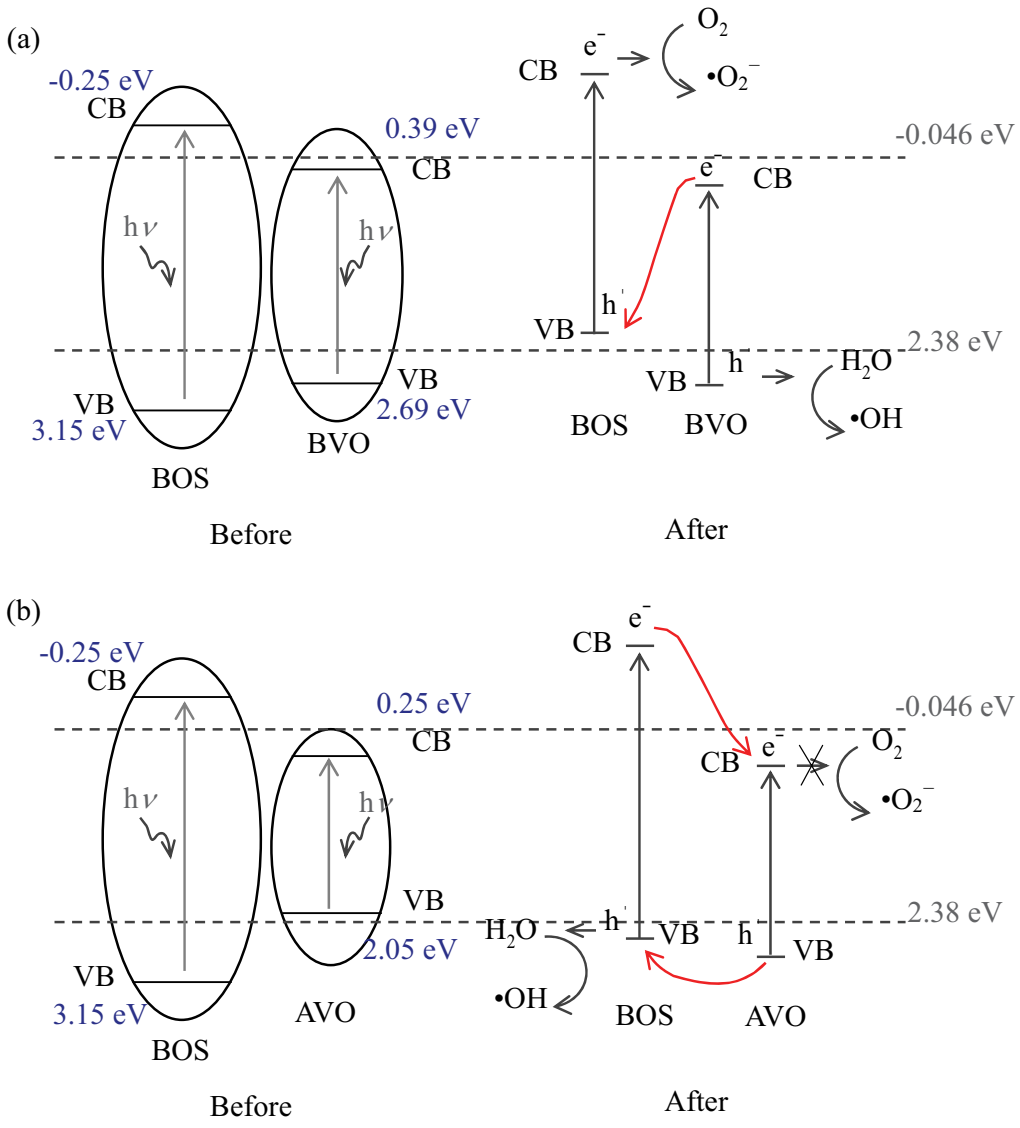

Fig. 10. Energy band diagram and possible charge-separation process (a) UV/BB2 and (b) UV/BA2.

pairs in the *p–n* heterojunction may significantly inhibit the recombination of the photo-generated charge carriers and extend their lifetime.

In Fig. 10a, the holes in the VB of BOS and the photo-generated electrons in the CB of BVO recombine directly at their interface. The photo-generated electrons in the CB of BOS are captured by the surface-chemisorbed O_2 to yield $^{\bullet}O_2^-$, while the remaining holes in BVO can directly degrade RR2. Since the CB edge potential of BOS is more negative than those of BVO and $O_2/^{\bullet}O_2^-$ (–0.046 V/NHE) [57], the photo-induced electrons may be trapped by the absorbed O_2, forming $^{\bullet}O_2^-$ [29]. Since the VB potential of BVO is more positive than the potential of $^{\bullet}OH/H_2O$ (2.38 V/NHE), h^+ can trap H_2O and OH^- and oxidize them to $^{\bullet}OH$. However, only a little of the absorbed H_2O and OH^- can be oxidized because most of the holes in the VB of BVO directly oxidize RR2. The findings herein suggest that the major active oxidation species in the UV/BB2 system are $^{\bullet}O_2^-$ and h^+.

In Fig. 10b, the photo-generated electrons in the CB of BOS are transferred to the CB of AVO, while holes in the VB of AVO are transferred to the VB of BOS. However, the CB potential of AVO is lower than the standard reduction potential of $O_2/^{\bullet}O_2^-$. The reactive species $^{\bullet}O_2^-$ cannot be formed in the UV/BA2 system. Since the VB potential of BOS is more positive than the potential of $^{\bullet}OH/H_2O$, holes can trap H_2O and OH^- and oxidize them to $^{\bullet}OH$. The proposed mechanisms in Fig. 10 are consistent with the results of the reactive species trapping experiments.

4. Conclusions

In this study, Vis.-induced BOS/BVO and BOS/AVO composites were synthesized by hydrothermal processes. The Vis. photocatalysis rates of the composites followed the order BA2 > BA1 > BB1 > BB2 > AVO > BVO > BOS. BB1 and BA1 were more active than a physical mixture of any pair of their constituent photocatalysts, revealing the importance of forming a heterojunction. The surface characteristics, Ag leaching, and photocatalysis results verified that coupling AVO with BOS increased the photocatalytic activity and reusability of AVO. The efficient separation of photo-generated electron–hole pairs in the *p–n* BOS/BVO and BOS/AVO heterojunctions considerably inhibited the recombination of the photo-generated charge carriers and extended their lifetime, increasing their photocatalytic activity.

Acknowledgments

The authors would like to thank the Ministry of Science and Technology and National Kaohsiung University of Science and Technology, for financially supporting this research under Contract No. MOST 107-2221-E-992-001-MY2 and 109B01, respectively.

References

[1] T.F. Chala, C.M. Wu, K.G. Motora, Rb_xWO_3/Ag_3VO_4 nanocomposites as efficient full-spectrum (UV, visible, and near-infrared) photocatalysis, J. Taiwan Inst. Chem. Eng., 102 (2019) 465–474.

[2] A. Malathi, J. Madhavan, A. Muthupandian, P. Arunachalam, A review on $BiVO_4$ photocatalyst: activity enhancement methods for solar photocatalytic applications, Appl. Catal., A, 555 (2018) 47–74.

[3] C.H. Wu, C.Y. Kuo, C.D. Dong, C.W. Chen, Y.L. Lin, W.M. Chen, Synthesis of $Bi_2O_3/BiVO_4$ heterojunction with enhanced photocatalytic activity via single-step hydrothermal method, Desal. Water Treat., 172 (2019) 417–427.

[4] C.H. Wu, C.Y. Kuo, C.D. Dong, C.W. Chen, Y.L. Lin, Y.S. Kuan, Synthesis, characterization and photocatalytic activity of a novel Bi_2O_3/Ag_3VO_4 heterojunction photocatalyst, Desal. Water Treat., 198 (2020) 364–375.

[5] C. Yu, D. Zeng, F. Chen, H. Ji, J. Zeng, D. Li, K. Yang, Construction of efficient solar-light-driven quaternary $Ag_3VO_4/Zn_3(VO_4)_2/Zn_2V_2O_7$/ZnO heterostructures for removing organic pollutants via phase transformation and *in-situ* precipitation route, Appl. Catal., A, 578 (2019) 70–82.

[6] F. Chen, C. Yu, L. Wei, Q. Fan, F. Ma, J. Zeng, J. Yi, K. Yang, H. Ji, Fabrication and characterization of $ZnTiO_3/Zn_2Ti_3O_8$/ZnO ternary photocatalyst for synergetic removal of aqueous organic pollutants and Cr(VI) ions, Sci. Total Environ., 706 (2020) 136026–136034, doi: 10.1016/j.scitotenv.2019.136026.

[7] T. He, D. Wu, Y. Tan, Fabrication of $BiOI/BiVO_4$ heterojunction with efficient visible-light-induced photocatalytic activity, Mater. Lett., 165 (2016) 227–230.

[8] N. Wetchakun, S. Chainet, S. Phanichphant, K. Wetchakun, Efficient photocatalytic degradation of methylene blue over $BiVO_4/TiO_2$ nanocomposites, Ceram. Int., 41 (2015) 5999–6001.

[9] O. Monfort, T. Roch, G. Maros, L. Satrapinskyy, D. Raptis, P. Lianos, G. Plesch, Photooxidative properties of various $BiVO_4/TiO_2$ layered composite films and study of their photocatalytic mechanism in pollutant degradation, J. Environ. Chem. Eng., 5 (2017) 5143–5149.

[10] M.F.R. Samsudin, S. Suriati, R. Bashiri, N.M. Mohamed, L.T. Siang, R.M. Ramli, Optimization of photodegradation of methylene blue over modified $TiO_2/BiVO_4$ photocatalysts: effects of total TiO_2 loading and different type of co-catalyst, Mater. Today: Proc., 5 (2018) 21710–21717.

[11] B. Samran, S. lunput, S. Tonnonchiang, S. Chaiwichian, $BiFeO_3/BiVO_4$ nanocomposite photocatalysts with highly enhanced photocatalytic activity for rhodamine B degradation under visible light irradiation, Physica B, 561 (2019) 23–28.

[12] T. Soltani, A. Tayyebi, B.K. Lee, $BiFeO_3/BiVO_4$ *p–n* heterojunction for efficient and stable photocatalytic and photoelectrochemical water splitting under visible-light irradiation, Catal. Today, 340 (2020) 188–196.

[13] S. Kaowphong, W. Choklap, A. Chachvalvutikul, N. Chandet, A novel $CuInS_2$/m-$BiVO_4$ *p-n* heterojunction photocatalyst with enhanced visible-light photocatalytic activity, Colloids Surf., A, 579 (2019) 123639–123649, doi: 10.1016/j.colsurfa.2019.123639.

[14] C. Lai, M. Zhang, B. Li, D. Huang, G. Zeng, L. Qin, X. Liu, H. Yi, M. Cheng, L. Li, Z. Chen, L. Chen, Fabrication of $CuS/BiVO_4$ (040) binary heterojunction photocatalysts with enhanced photocatalytic activity for ciprofloxacin degradation and mechanism insight, Chem. Eng. J., 358 (2019) 891–902.

[15] P. Ju, P. Wang, B. Li, H. Fan, S. Ai, D. Zhang, Y. Wang, A novel calcined $Bi_2WO_6/BiVO_4$ heterojunction photocatalyst with highly enhanced photocatalytic activity, Chem. Eng. J., 236 (2014) 430–437.

[16] N. Omrani, A. Nezamzadeh-Ejhieh, A comprehensive study on the mechanism pathways and scavenging agents in the photocatalytic activity of $BiVO_4/WO_3$ nano-composite, J. Water Process Eng., 33 (2020) 101094–101104, doi: 10.1016/j.jwpe.2019.101094.

[17] X. Xiang, Y. Wang, P. Ju, L. Yang, D. Zhang, Facile fabrication of $AgI/BiVO_4$ composites with enhanced visible photocatalytic degradation and antibacterial ability, J. Alloys Compd., 721 (2017) 622–627.

[18] S. Obregon, E.D. Barriga-Castro, R. Mendoza-Resendez, C. Luna, Enhanced photocatalytic behavior of $BiVO_4$ through photoinduced charge transfer to amorphous β-FeOOH nanoparticles, Ceram. Int., 42 (2016) 17773–17780.

[19] J. Li, W. Zhao, G. Yang, Z. Wei, M. Han, H. He, S. Yang, C. Sun, Facile synthesis and high activity of novel $BiVO_4/FeVO_4$ heterojunction photocatalyst for degradation of metronidazole, Appl. Surf. Sci., 351 (2015) 270–279.

[20] U. Lamdab, K. Wetchakunb, S. Phanichphant, W. Kangwansupamonkond, N. Wetchakun, $InVO_4$-$BiVO_4$ composite films with enhanced visible light performance for photodegradation of methylene blue, Catal. Today, 278 (2016) 291–302.
[21] D. Mitoraja, U. Lamdab, W. Kangwansupamonkon, M. Pacia, W. Macyk, N. Wetchakun, R. Beranek, Revisiting the problem of using methylene blue as a model pollutant in photocatalysis: the case of $InVO_4$/$BiVO_4$ composites, J. Photochem. Photobiol., A, 366 (2018) 103–110.
[22] L. Song, Y. Pang, Y. Zheng, C. Chen, L. Ge, Design, preparation and enhanced photocatalytic activity of porous BiOCl/$BiVO_4$ microspheres via a coprecipitation-hydrothermal method, J. Alloys Compd., 710 (2017) 375–382.
[23] S. Selvarajan, A. Suganthi, M. Rajarajan, K. Arunprasath, Highly efficient $BiVO_4$/WO_3 nanocomposite towards superior photocatalytic performance, Powder Technol., 307 (2017) 203–212.
[24] A. Malathi, V. Vasanthakumar, A. Prabhakarn, J. Madhavan, M.A. Ghanem, A low cost additive-free facile synthesis of $BiFeWO_6$/$BiVO_4$ nanocomposite with enhanced visible-light induced photocatalytic activity, J. Colloid Interface Sci., 506 (2017) 553–563.
[25] L. Li, B. Yan, $BiVO_4$/Bi_2O_3 submicrometer sphere composite: microstructure and photocatalytic activity under visible-light irradiation, J. Alloys Compd., 476 (2009) 624–628.
[26] M. Mao, F. Chen, C. Zheng, J. Ning, Y. Zhong, Y. Hu, Facile synthesis of porous Bi_2O_3-$BiVO_4$ *p–n* heterojunction composite microrods with highly efficient photocatalytic degradation of phenol, J. Alloys Compd., 688 (2016) 1080–1087.
[27] Q. Shi, W. Zhao, L. Xie, J. Chen, M. Zhang, Y. Li, Enhanced visible-light driven photocatalytic mineralization of indoor toluene via a $BiVO_4$/reduced graphene oxide/Bi_2O_3 all-solid-state Z-scheme system, J. Alloys Compd., 662 (2016) 108–117.
[28] P. Qiu, B. Park, J. Choi, M. Cui, J. Kim, J. Khim, $BiVO_4$/Bi_2O_3 heterojunction deposited on graphene for an enhanced visible-light photocatalytic activity, J. Alloys Compd., 706 (2017) 7–15.
[29] J. Sun, X. Li, Q. Zhao, M.O. Tade, S. Liu, Construction of *p–n* heterojunction β-Bi_2O_3/$BiVO_4$ nanocomposite with improved photoinduced charge transfer property and enhanced activity in degradation of ortho-dichlorobenzene, Appl. Catal., B, 219 (2017) 259–268.
[30] Y. Lee, M. Cui, J. Choi, J. Kim, Y. Son, J. Khim, Degradation of polychlorinated dibenzo-p-dioxins and dibenzofuransin real-field soil by an integrated visible-light photocatalysis and solvent migration system with *p–n* heterojunction $BiVO_4$/Bi_2O_3, J. Hazard. Mater., 344 (2018) 1116–1125.
[31] L. Cao, K. Xu, R. Wang, Ag_2S nanoparticles decorated $BiVO_4$ composites: 3-mercaptopropionic acid assisted synthesis and enhanced visible-light-driven photocatalytic performance, Mater. Res. Bull., 113 (2019) 175–181.
[32] W. Zhao, Y. Feng, H. Huang, P. Zhou, J. Li, L. Zhang, B. Dai, J. Xu, F. Zhu, N. Sheng, D.Y.C. Leung, A novel Z-scheme Ag_3VO_4/$BiVO_4$ heterojunction photocatalyst: study on the excellent photocatalytic performance and photocatalytic mechanism, Appl. Catal., B, 245 (2019) 448–458.
[33] W. Kanlayawat, P. Sukon, T. Doldet, I. Burapat, $CoTiO_3$/Ag_3VO_4 composite: a study on the role of $CoTiO_3$ and the active species in the photocatalytic degradation of methylene blue, J. Colloid Interface Sci., 454 (2015) 210–215.
[34] Y. Xie, Y. Dai, X. Yuan, L. Jiang, L. Zhou, Z. Wu, J. Zhang, H. Wang, T. Xiong, Insight on the plasmonic Z-scheme mechanism underlying the highly efficient photocatalytic activity of silver molybdate/silver vanadate composite in rhodamine B degradation, J. Colloid Interface Sci., 530 (2018) 493–504.
[35] L. Zhang, Y. He, P. Ye, W. Qin, Y. Wu, T. Wu, Enhanced photodegradation activity of Rhodamine B by Co_3O_4/Ag_3VO_4 under visible light irradiation, Mater. Sci. Eng., B, 178 (2013) 45–52.
[36] V.R. Raja, D.R. Rosaline, A. Suganthi, M. Rajarajanc, Ultrasonic assisted synthesis with enhanced visible-light photocatalytic activity of NiO/Ag_3VO_4 nanocomposite and its antibacterial activity, Ultrason. Sonochem., 44 (2018) 73–85.
[37] T. Zhu, Y. Song, H. Ji, Y. Xu, Y. Song, J. Xia, S. Yin, Y. Li, H. Xu, Q. Zhang, H. Li, Synthesis of g-C_3N_4/Ag_3VO_4 composites with enhanced photocatalytic activity under visible light irradiation, Chem. Eng. J., 217 (2015) 96–105.
[38] L. Zhang, Y. He, P. Ye, Y. Wu, T. Wu, Enhanced photodegradation activity of Rhodamine B by $MgFe_2O_4$/Ag_3VO_4 under visible light irradiation, Catal. Commun., 30 (2013) 14–18.
[39] B. Inceesungvorn, T. Teeranunpong, J. Nunkaew, S. Suntalelat, D. Tantraviwat, Novel $NiTiO_3$/Ag_3VO_4 composite with enhanced photocatalytic performance under visible light, Catal. Commun., 54 (2014) 35–38.
[40] J. Zhang, Z. Ma, Enhanced visible-light photocatalytic performance of Ag_3VO_4/Bi_2WO_6 heterojunctions in removing aqueous dyes and tetracycline hydrochloride, J. Taiwan Inst. Chem. Eng., 78 (2017) 212–218.
[41] J. Zhang, Z. Ma, Ag_3VO_4/$BiOIO_3$ heterojunction with enhanced visible-light-driven catalytic activity, J. Taiwan Inst. Chem. Eng., 88 (2018) 177–185.
[42] M. Su, C. He, V.K. Sharma, M.A. Asi, D. Xia, X.Z. Li, H. Deng, Y. Xiong, Mesoporous zinc ferrite: synthesis, characterization, and photocatalytic activity with H_2O_2/visible light, J. Hazard. Mater., 211–212 (2012) 95–103.
[43] M.S. Gui, W.D. Zhang, Q.X. Su, C.H. Chen, Preparation and visible light photocatalytic activity of Bi_2O_3/Bi_2WO_6 heterojunction photocatalysts, J. Solid State Chem., 184 (2011) 1977–1982.
[44] H. Huang, K. Liu, K. Chen, Y. Zhang, Y. Zhang, S. Wang, Ce and F comodification on the crystal structure and enhanced photocatalytic activity of Bi_2WO_6 photocatalyst under visible light irradiation, J. Phys. Chem. C, 118 (2014) 14379–14387.
[45] Y. Chen, S. Yang, K. Wang, L. Lou, Role of primary active species and TiO_2 surface characteristic in UV-illuminated photodegradation of Acid Orange 7, J. Photochem. Photobiol., A, 172 (2005) 47–54.
[46] Q. Guo, Y. Huang, H. Xu, D. Luo, F. Huang, L. Gu, Y. Wei, H. Zhao, L. Fan, J. Wu, The effects of solvent on photocatalytic properties of Bi_2WO_6/TiO_2 heterojunction under visible light irradiation, Solid State Sci., 78 (2018) 95–106.
[47] L. Yuan, K.Q. Lu, F. Zhang, X. Fu, Y.J. Xu, Unveiling the interplay between light-driven CO_2 photocatalytic reduction and carbonaceous residues decomposition: a case study of Bi_2WO_6-TiO_2 binanosheets, Appl. Catal., B, 237 (2018) 424–431.
[48] S. Wang, Y. Guan, L. Wang, W. Zhao, H. He, J. Xiao, S. Yang, C. Sun, Fabrication of a novel bifunctional material of BiOI/Ag_3VO_4 with high adsorption–photocatalysis for efficient treatment of dye wastewater, Appl. Catal., B, 168–169 (2015) 448–457.
[49] Y. Shi, L. Luo, Y. Zhang, Y. Chen, S. Wang, L. Li, Y. Long, F. Jiang, Synthesis and characterization of α/β-Bi_2O_3 with enhanced photocatalytic activity for 17α-ethynylestradiol, Ceram. Int., 43 (2017) 7627–7635.
[50] J. Zeng, J. Zhong, J. Li, Z. Xiang, X. Liu, J. Chen, Improvement of photocatalytic activity under solar light of $BiVO_4$ microcrystals synthesized by surfactant-assisted hydrothermal method, Mater. Sci. Semicond. Process., 27 (2014) 41–46.
[51] D.H. Cui, Y.F. Zheng, X.C. Song, A novel visible-light-driven photocatalyst Ag_2O/AgI with highly enhanced photocatalytic performances, J. Alloys Compd., 701 (2017) 163–169.
[52] S. Akel, R. Dillert, N.O. Balayeva, R. Boughaled, J. Koch, M.E. Azzouzi, D.W. Bahnemann, Ag/Ag_2O as a co-catalyst in TiO_2 photocatalysis: effect of the co-catalyst/photocatalyst mass ratio, Catalysts, 8 (2018) 647–665, doi: 10.3390/catal8120647.
[53] X. Ma, Z. Ma, T. Liao, X. Liu, Y. Zhang, L. Li, W. Li, B. Hou, Preparation of $BiVO_4$/BiOCl heterojunction photocatalyst by *in-situ* transformation method for norfloxacin photocatalytic degradation, J. Alloys Compd., 702 (2017) 68–74.
[54] L. Chen, Q. Zhang, R. Huang, S.F. Yin, S.L. Luo, C.T. Au, Porous peanut-like Bi_2O_3-$BiVO_4$ composites with heterojunctions: one-step synthesis and their photocatalytic properties, Dalton Trans., 41 (2012) 9513–9518.

[55] X. Meng, Z. Zhang, Bismuth-based photocatalytic semiconductors: introduction, challenges and possible approaches, J. Mol. Catal. A: Chem., 423 (2016) 533–549.
[56] S. Li, S. Hu, W. Jiang, Y. Liu, J. Liu, Z. Wang, Facile synthesis of flower-like Ag_3VO_4/Bi_2WO_6 heterojunction with enhanced visible-light photocatalytic activity, J. Colloid Interface Sci., 501 (2017) 156–163.
[57] N. Tian, H. Huang, Y. He, Y. Guo, T. Zhang, Y. Zhang, Mediator-free direct Z-scheme photocatalytic system: $BiVO_4$/g-C_3N_4 organic-inorganic hybrid photocatalyst with highly efficient visible-light-induced photocatalytic activity, Dalton Trans., 44 (2015) 4297–4307.